Constraint of non-methane volatile organic compound emissions with TROPOMI HCHO observations and its impact on summertime surface ozone simulation over China

Shuzhuang Feng[1], Fei Jiang[1,2,5*], Tianlu Qian[3], Nan Wang[4], Mengwei Jia[1], Songci Zheng[1], Jiansong Chen[6], Fang Ying[6], Weimin Ju[1,2]

[1] *Jiangsu Provincial Key Laboratory of Geographic Information Science and Technology, International Institute for Earth System Science, Nanjing University, Nanjing, 210023, China*

[2] *Jiangsu Center for Collaborative Innovation in Geographical Information Resource Development and Application, Nanjing, 210023, China*

[3] *School of Geographic and Biologic Information, Nanjing University of Postsand Telecommunications, Nanjing, 210023, China*

[4] *College of Carbon Neutrality Future Technology, Sichuan University, Chengdu, 610207, China*

[5] *Frontiers Science Center for Critical Earth Material Cycling, Nanjing University, Nanjing, 210023, China*

[6] *Hangzhou Municipal Ecology and Environment Bureau, Hangzhou, 310020, China*

* Corresponding author: Tel.: +86-25-83597077; Fax: +86-25-83592288; E-mail address: jiangf@nju.edu.cn

Text S1

Figure S1 shows the spatial distribution of temporally averaged prior and posterior emissions, along with their differences in emissions for August 2022. Higher emissions were predominantly concentrated in central and eastern China, especially in the NCP, Yangtze River Delta (YRD), and PRD, all of which are significant industrial or high-density urban areas. Lower emissions were primarily occurred across Northwest and Southern China. Compared with the prior emissions, posterior NO_x emissions exhibited a significant decrease in the NCP, YRD, and parts of Central China. Furthermore, it was observed that most key urban areas tended to have their emissions overestimated in the prior inventory, while their surrounding areas had their emissions underestimated. Owing to the absence of precise emission location data, spatial proxies like population density, GDP, and road networks, are utilized for allocating total emissions across residential, industrial, and transportation emission sectors, which introduces uncertainties in spatial disaggregation. Overall, the total national NO_x emissions decreased by 10.2% to 47.3 Gg in the posterior emissions. This disparity arises from uncertainties in the prior inventory and changes in China's NO_x emissions reduction from 2020 to 2022.

Test S2

Meteorological processes play a dominant role in the transport, mixing, and chemical reactions of pollutants. Therefore, their simulation accuracy significantly affects emission inversion. To evaluate the performance of WRF simulations quantitatively, we utilized the surface meteorological measurements from 400 stations with 3-hour intervals, including temperature at 2 m (T2), relative humidity at 2 m (RH2), and wind speed at 10 m (WS10), and planetary boundary layer height (PBLH) measured by sounding from 84 stations with 12-hour intervals in this study. These surface and sounding data were obtained from the National Climate Data Center (NCDC) integrated surface database (http://www.ncdc.noaa.gov/oa/ncdc.html, last access: 25 May 2022) and the website of the University of Wyoming (http://weather.uwyo.edu/upperair/sounding.html, last access: 25 May 2022), respectively. The observed PBLH were calculated through the bulk Richardson number method with sounding data. Here, three basic statistical measures, mean bias, root-mean-square error (RMSE), and correlation coefficient (CORR), are applied to evaluate the results (Table S3). The results showed that the WRF model satisfactorily reproduced T2, RH2, WS10, and PBLH (Figure S9), with small biases of -0.5 °C, -5.3%, 0.3 m/s, and -42.4 m, respectively.
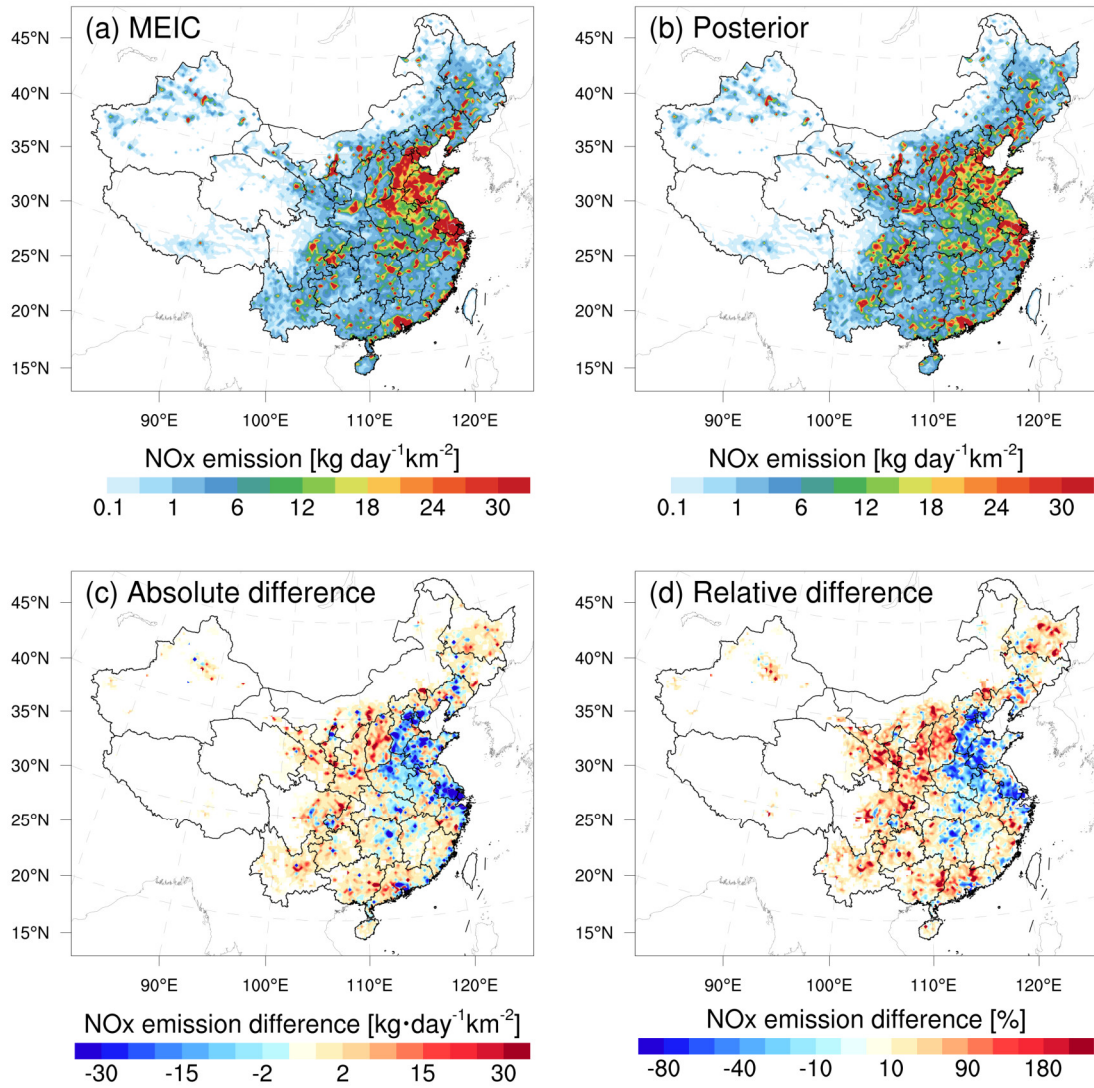
Figure S1. Spatial distribution of the time-averaged (a) prior emissions (MEIC 2020), (b) posterior emissions, (c) absolute difference (posterior minus MEIC), and (d) relative difference of NO$_x$ over China.
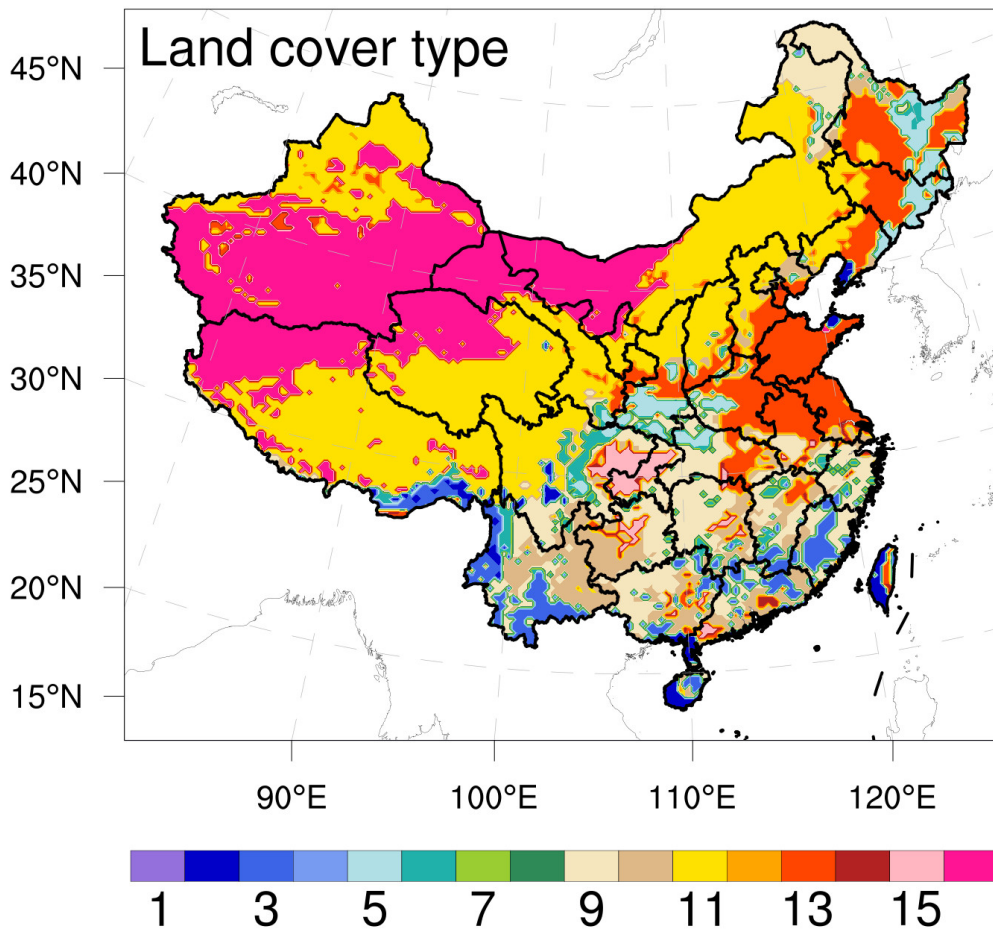
Figure S2. Combined MODIS International Geosphere-Biosphere Programme (IGBP) data from the MCD12C1 product, 2020 (https://lpdaac.usgs.gov/products/mcd12c1v061/). 1, Evergreen needleleaf forests; 2, Evergreen broadleaf forests; 3, Deciduous needleleaf forests; 4, Deciduous broadleaf forests; 5, Mixed forests; 6, Closed shrublands; 7, Open shrublands; 8, Woody savannas; 9, Savannas; 10, Grasslands; 11, Permanent wetlands; 12, Croplands; 13, Urban and built-up; 14, Cropland-natural vegetation mosaics; 15, Snow and ice; 16, Sparsely vegetated.
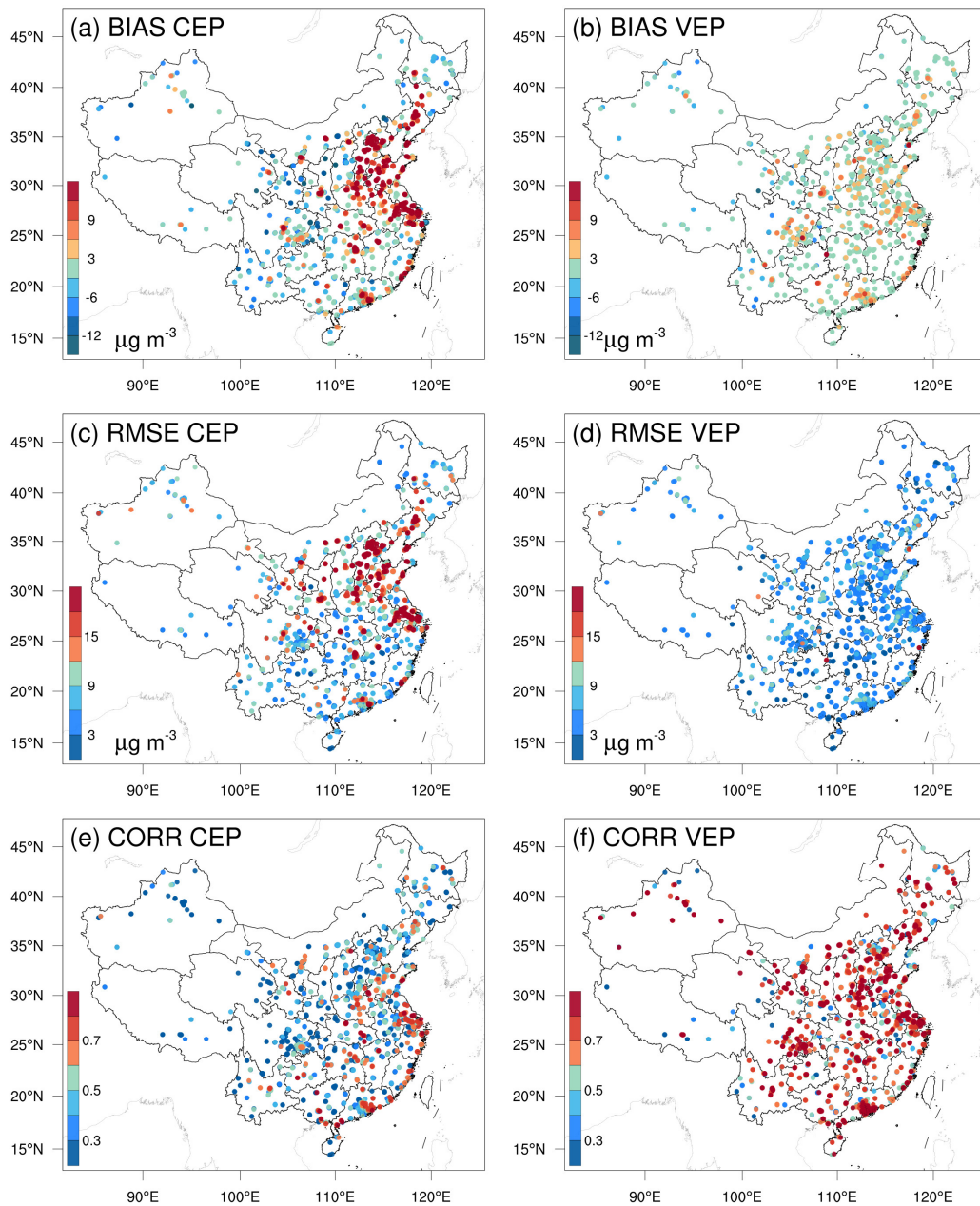
Figure S3. Spatial distribution of mean bias (BIAS, a and b), root mean square error (RMSE, c and d), and correlation coefficient (CORR, e and f) for simulated NO$_2$ using prior (left, CEP) and posterior (right, VEP) emissions, respectively.
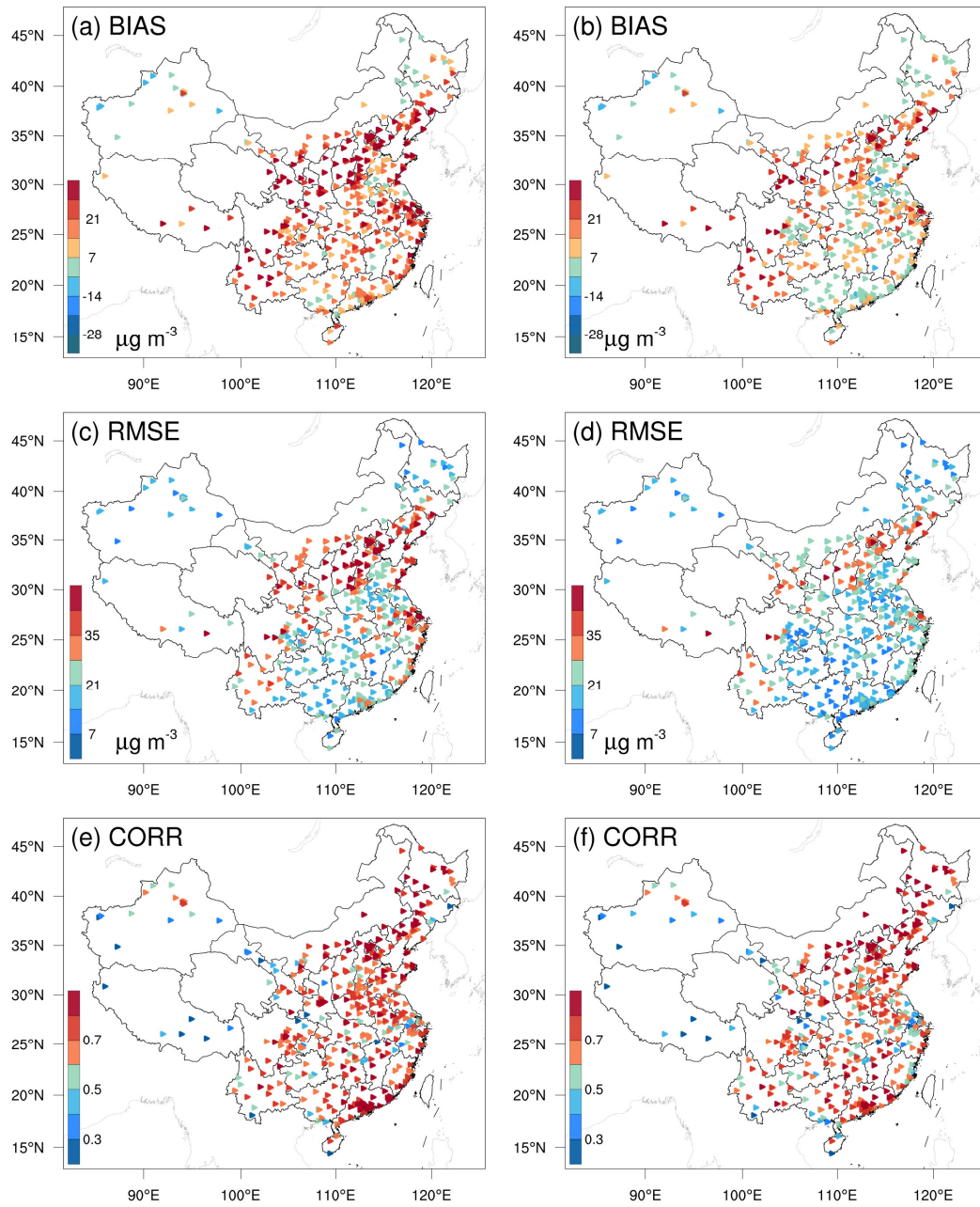
Figure S4. Spatial distribution of mean bias (BIAS, a and b), root mean square error (RMSE, c and d), and correlation coefficient (CORR, e and f) for simulated O₃ using prior (left, CEP1) and posterior (right, VEP) emissions against independent observations.
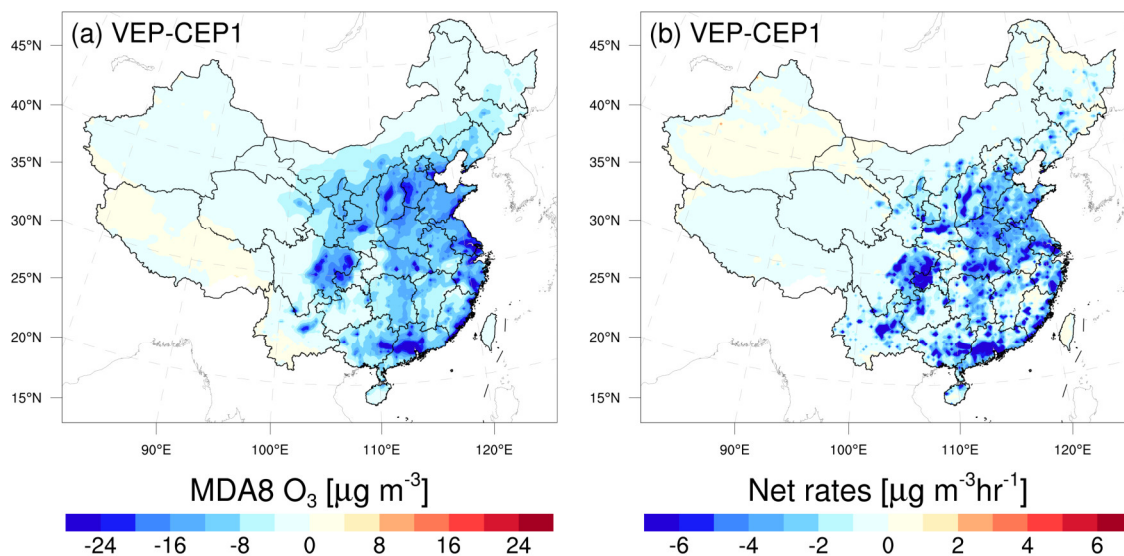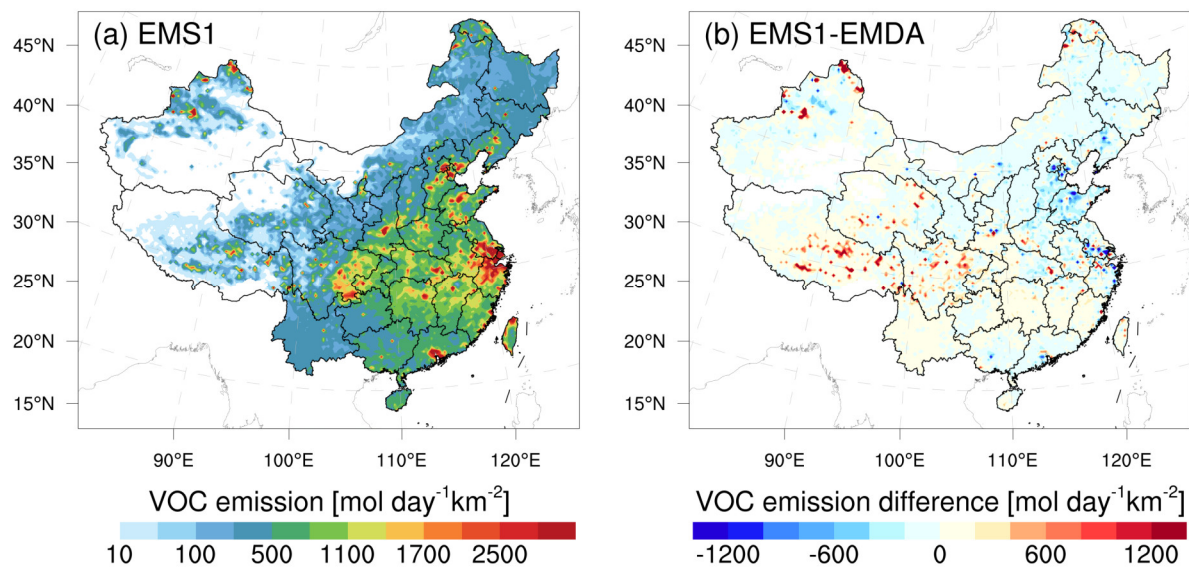
Figure S5. Differences in simulated (a) maximum daily 8-hour average (MDA8) O_3 concentrations and (b) net reaction rates between CEP1 and VEP experiments.
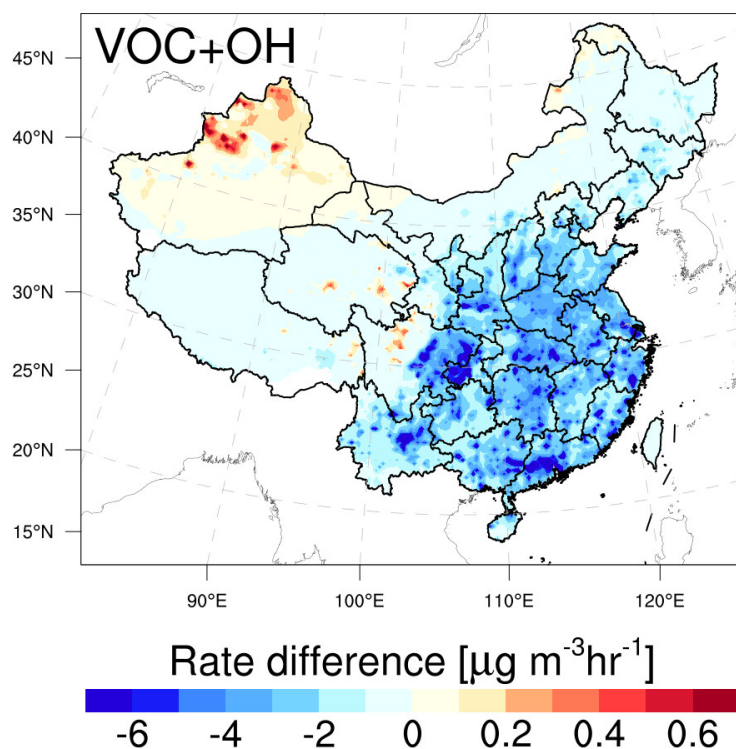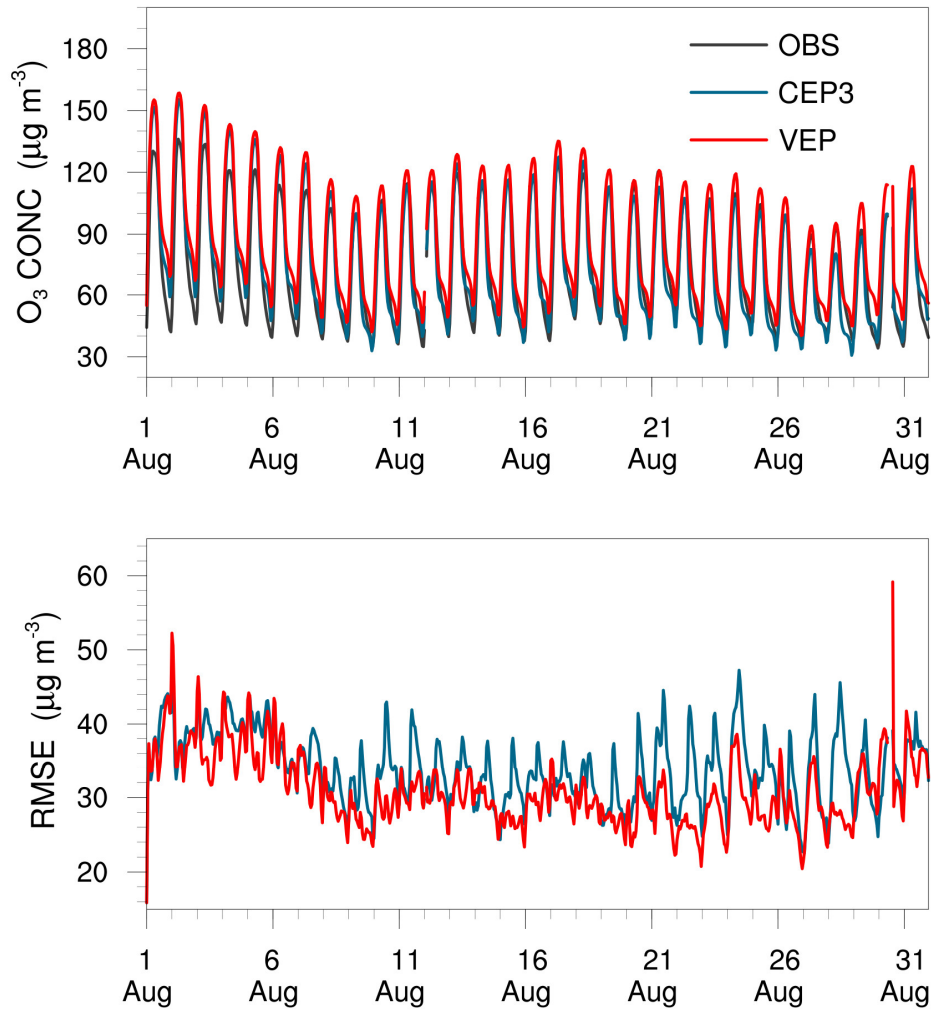

Figure S6. Differences in reaction rates of VOC + OH between CEP1 and VEP experiments at the surface. Time period: August 2022, 12:00–18:00 CST.

Figure S7. Spatial distribution of the time-averaged (a) posterior emissions in EMS1 and (b) differences in posterior emissions between EMS1 and EMDA (EMS1-EMDA). EMS1 increased background error from 40% to 80% compared to EMDA.

Figure S8. Time series of (a) hourly surface O₃ concentrations (μg m⁻³) and (b) RMSE (μg m⁻³) obtained from VEP and CEP3 experiments, CEP3 was simulated using the posterior emissions disregarding the uncertainty in NOₓ emissions.
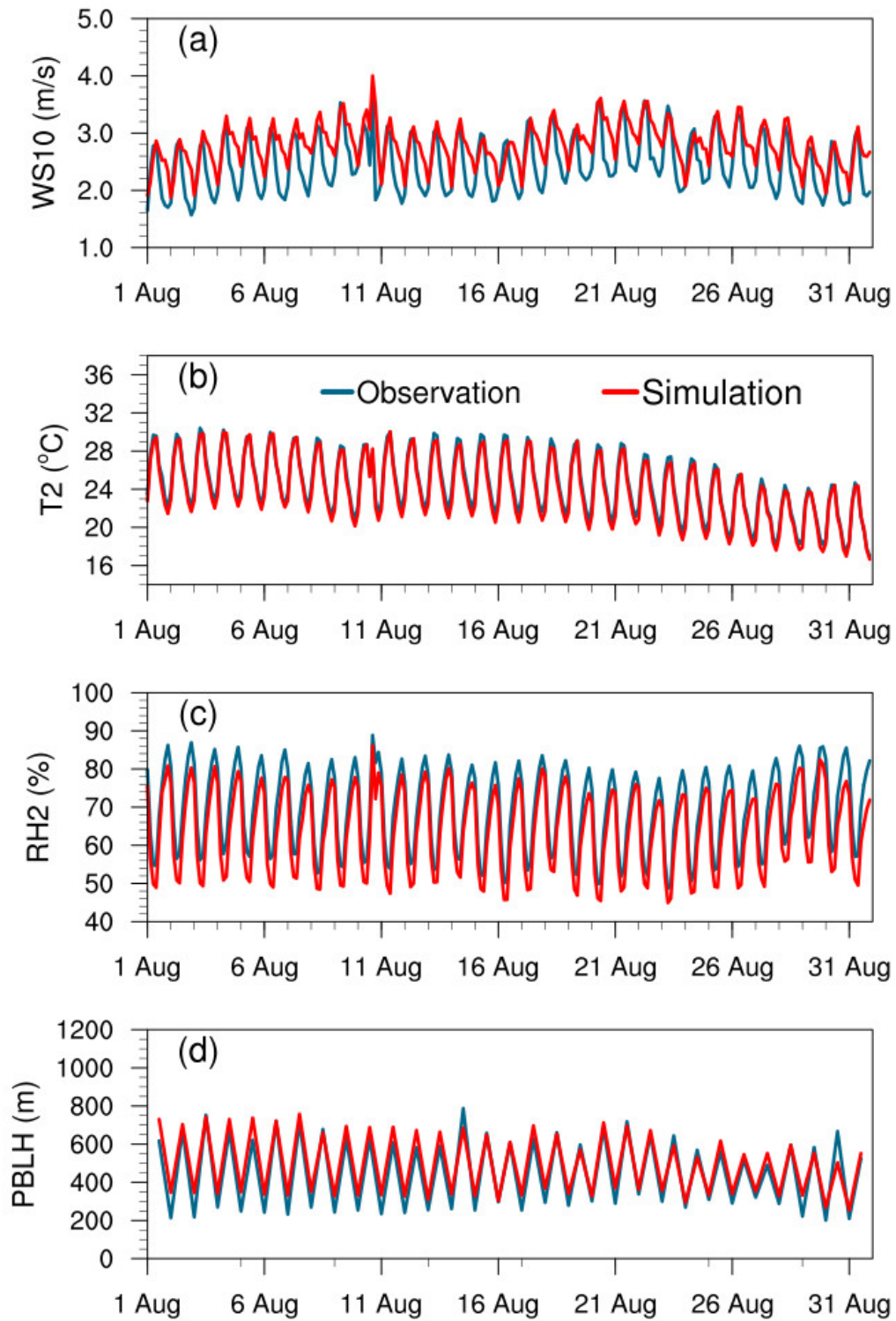
Figure S9. Time series of observed and simulated wind speeds at 10 m (WS10, m/s), temperature at 2 m (T2, ℃), relative humidity at 2 m (RH2, %), and planetary boundary layer height (PBLH, m) over mainland China.

Table S1. Configuration options of WRF/CMAQ

WRF		CMAQ	
Parameter	Scheme	Parameter	Scheme
Microphysics	WSM6	Horizontal/Vertical advection	yamo/wrf
Longwave	RRTM	Horizontal/Vertical diffusion	multiscale/acm2
Shortwave	Goddard	Deposition	m3dry
Boundary layer	ACM	Chemistry solver	EBI
Cumulus	Kain-Fritsch	Photolysis	phot_inline
Land-surface	Noah	Aerosol module	AERO6
Surface layer	Revised	Cloud module	cloud_acm_ae6
Urban canopy	No	Gas-phase chemistry	CB05tucl

Table S2. Statistics comparison of simulated and observed 10-m wind speed (WS10), 2-m temperature (T2), 2-m relative humidity (RH2), and planetary boundary layer height (PBLH).

Variable Met.	No. of sites	Mean Obs.	Mean Sim.	BIAS	RMSE	CORR
WS10 (m/s)	400	2.5	2.8	0.3	0.5	0.73
T2 (°C)	400	24.5	24.0	-0.5	0.6	1.00
RH2 (%)	400	69.0	63.8	-5.3	5.5	0.99
PBLH (m)	84	451.2	493.6	42.4	68.6	0.96

* BIAS, mean bias; RMSE, root mean square error; CORR, correlation coefficient